Numerical investigation of an innovative furnace concept for industrial coil coating lines

Bruno A.C. Barata [a], Beatriz S. Dias [a], Jorge E.P. Navalho [a,b,*], Michael Schneider [c], Petra Weinbrecht [c], Christof Weis [c], Dimosthenis Trimis [c], José C.F. Pereira [a]

[a] IDMEC, Instituto Superior Técnico, Universidade de Lisboa, Lisboa, 1049-001, Portugal
[b] Departamento de Engenharia Mecânica e Industrial, Faculdade de Ciências e Tecnologia, Universidade Nova de Lisboa, Caparica, 2829-516, Portugal
[c] Engler-Bunte-Institute, Divison of Combustion Technology, Karlsruhe Institute of Technology, Karlsruhe, 76131, Germany

ARTICLE INFO

ABSTRACT

In this work, the engineering performance of an innovative furnace concept developed for continuous drying and curing of paint-coated metal sheets (coil coating process) is investigated through advanced modeling and numerical simulation techniques. Unlike the traditional and wide-spread coil coating furnaces – which operate according to the so-called convective air-drying technology –, the present furnace concept relies on infrared radiative heating to drive solvent evaporation and curing reactions. Radiative heat is provided by the operation of radiant porous burners which are fed with evaporated solvents. The current furnace concept consists of two main chambers (the radiant burner section and the curing oven section) with different gas compositions (atmospheres) that are separated by a semi-transparent window. The window allows energy transfer and prevents gas mixing between the two sections. To utilize the solvent-loaded atmosphere available in the curing oven section as fuel – and to prevent the development of explosive conditions therein –, a novel inertization concept shielding the curing oven section from the external environment is considered. The current furnace concept aims at improving process intensification and promoting energy efficiency. For the current furnace concept, numerical simulation results support a suitable and competitive performance for drying the applied coatings in comparison with the traditional approach. Simultaneously, a safe operation is predicted, without (i) solvent leakage from the furnace and (ii) oxygen entrainment from the surrounding ambient into the furnace. These conditions are satisfied demonstrating a safe operation and a complete evaporation of solvents from applied liquid film coatings.

1. Introduction

The coil coating industrial process is applied to improve the features of bare metal substrates – particularly, steel and aluminum –, such as the resistance to corrosion and aesthetics (appearance) and to provide additional functions namely enhanced optical properties for energy saving concerns on customer final (end-use) applications [1–5]. Coated metal coils find applications in many sectors, such as in building construction (facades, cladding, roofs, *etc.*), automotive industry, and in the manufacturing of furniture and household appliances [1,4,6]. Metal substrates to be coated are provided to a coil coating line as a continuous thin and flat metal strip previously unwound from a coil. The drying/curing stage of the liquid film (paint) that is applied onto the surfaces of the metal strip – a central (and highly energy intensive) step in coil coating lines – is conventionally carried out in large ovens

fed with a heated air stream that provides the required energy (by convective heat transfer) for the process and carries away the evaporated solvents (volatile organic compounds) from the oven [1,7].

Previous research on coil coating available in the open literature has been mainly concerned with the development of new coating formulations and drying/curing technologies. Coating formulations have been investigated for improving the performance of drying and curing processes, namely through novel NIR (near infrared) technologies [8–10], for improving the final product optical properties, such as the solar reflectance and thermal emittance (cool coating applications) [11,12], and for reducing the utilization of VOCs (volatile organic compounds) through the development of bio-based reactive diluents [6,13]. The development of drying and curing technologies has been mainly motivated by energy efficiency concerns. Particularly, great interest has been observed in applying infrared (IR) radiant heat to support solvents

evaporation and coating curing – replacing the conventional air-drying technology strongly based on convective heat transfer [9,14,15]. Accordingly, by applying a radiative heat source – through suitable lamps or radiant burners – smaller ovens, lower residence times of the coil in the oven, higher line speeds, higher energy efficiency, and large production capacity can be achieved [15].

As far as the authors are aware, the open literature is very scarce on full performance characterization studies of coil coating ovens, in particular, innovative concepts that break with the traditional convective air-drying technology. Brennan et al. [16] applied the transient two-dimensional heat diffusion equation coupled with suitable boundary conditions to investigate the thermal performance of spectrally selective coatings in an industrial NIR furnace featured with tungsten–halogen filaments. However, full CFD (computational fluid dynamics) numerical predictions for the aero-thermal performance of the entire furnace – needed to characterize in detail convective heat and mass transfer rates – were addressed to future work. Neno et al. [17] studied the heat removal capability from a semi-transparent glass window partition for a radiative coil coating oven applying the heat diffusion equation along the thickness of the glass slab and Nusselt number correlations – to compute convection heat transfer coefficients – that were specifically derived by CFD numerical simulations considering window cooling by wall jets. Dias et al. [18] developed a multi-scale methodology to predict the drying behavior of a coated substrate under IR radiant burners. Their methodology couples a CFD model (macro-scale model) – to predict the heat and mass convection and net radiative heat transfer rates in the furnace – with a drying film model (micro-scale model) to compute the temperature, composition, and thickness of the coating along the residence time in the furnace. Yuan et al. [19] investigated experimentally the application of catalytic burners for providing the IR radiation for curing powder coatings. Additionally, they have considered a one-dimensional model to predict the temperature distribution along the thickness of the substrate–coating system. While these works are related to IR ovens applicable to coil coating, most of them have only considered a part (subsystem) of the entire furnace and have not provided a thorough performance investigation for a fully functional coil coating oven.

This work presents a novel radiative coil coating furnace concept that not only improves the system compactness and energy efficiency but also boosts production flexibility. The overall performance of the innovative coil coating furnace operating with radiant porous burners is herein numerically investigated considering three different operating conditions – two extreme conditions and a nominal operating condition. Particularly, through a three-dimensional (3D) model of the full-scale (entire) furnace, the furnace thermal behavior and the furnace sealing proof (atmosphere shielding) are fully addressed in order to assess the feasibility for a long-term safe, stable, and ultimately, successful furnace operation. The irradiation distribution at the coil top surface is analyzed to evaluate the available energy for coating processing. The heating performance of uncoated and coated metallic samples in a properly developed small-scale (pilot) furnace model is evaluated through a two-dimensional (2D) model and compared with the corresponding experimental results. Additionally, solvent evaporation from applied liquid film coatings onto metallic samples with the current furnace concept is evaluated considering the small- and full-scale 2D furnace models.

This paper is organized as follows. After the short introduction provided in this section (Section 1) – where the research topic, its relevance, as well as the motivation and objectives of the current study are presented –, the section that follows (Section 2) describes in detail the novel coil coating furnace concept. Section 3 presents the physical, mathematical, and numerical models, the boundary conditions that match the furnace operating conditions, and the computational mesh features. The results and accompanying discussion are presented afterwards (Section 4). Finally, this paper ends in Section 5 with summary conclusions.

2. Coil coating furnace concept

Fig. 1 presents the schematic representation of the complete radiative coil coating furnace. According to the current furnace concept, the required energy to trigger and support the coating drying and curing stages is provided by the operation of radiant porous burners. This burners are fed with solvent species evaporated from the wet coating applied onto the metal strip (coil) surface. The coil coating furnace is mainly composed by two thermally coupled modules: the radiant burner section (RBS) and the curing oven section (COS) – see Fig. 1. The RBS is placed at the top of the COS module. The outlet section of radiant porous burners (ceramic open-cell foam structures glowing during burners operation) – that provide the IR (infrared) radiant heat for coating processing – is placed at the ceiling of the RBS facing towards the COS where a coated metal strip is continuously passing through. In between both modules, a glass window partition is applied to avoid mixing RBS and COS atmospheres, and simultaneously, to allow a net radiative heat transfer from the burners surfaces (located at in RBS) to the paint film (located in the COS). According to this configuration, the RBS atmosphere is composed by the burners flue gas while the COS atmosphere is composed by a solvent-rich mixture (volatile species released from wet coatings during drying). The COS gas mixture is extracted and directed to the porous burners feeding system — see the extraction section at the bottom of the COS (Fig. 1).
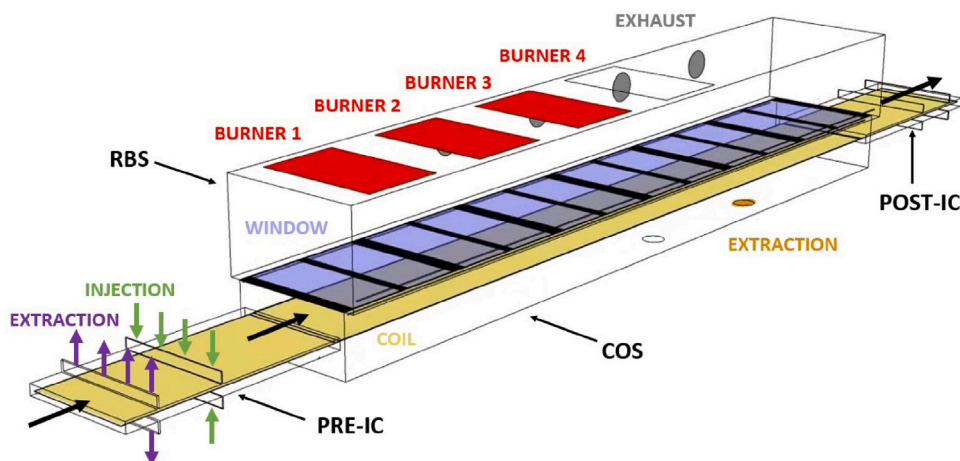

Fig. 1. Schematic representation of the proposed radiative coil coating furnace concept. (IC — inertization chamber; RBS — radiant burner section; and COS — curing oven section.).

This integrated solution that simultaneously eliminates VOCs and takes advantage of its thermal energy content results in an overall compact and energy efficient system. Otherwise, as in traditional coil coating lines, solvents would have to be incinerated in external bulky and costly equipment (incinerators or oxidative thermal regenerators) where a significant amount of the solvents energetic value would be wasted.

Since the COS is constantly crossed by the metal strip, the corresponding openings (slits) – that allow the metal strip entrance and exit – constitute a problematic issue to ensuring the COS atmosphere sealing. To overcome such issue and prevent any leakage from the COS atmosphere, as well as any external (surrounding) air entrainment to the COS, inertization chambers (a gaseous sealing concept) are applied at the COS entrance and exit sections of the metal strip. In the inertization chambers, flue gas from the burners is injected near the COS entrance/exit section towards the metal strip (impinging plane jets) and extracted through slots located near the sections of the inertization chambers with the surrounding environment — see in Fig. 1 the green and purple set of arrows (above and below the metal strip) illustrating the injection and extraction streams, respectively, for the pre-inertization chamber. The flue gas injected and extracted in the pre- and post-inertization chambers (pre- and post-IC) behaves as a gaseous curtain between the external environment and the COS region, shielding the COS atmosphere. The window partition that separates the RBS and COS atmospheres is a fundamental component of the furnace. The window is subjected to very harsh thermal conditions due to the absorption of a fraction of the total radiative power emitted by the radiant porous burners, due to the temperature difference that establishes between the two separated atmospheres, and due to the impingement of hot burners flue gas at the window top surface. To attenuate these effects on the window thermal behavior, a cooling system based on wall jet cooling is considered. In particular, near the window top surface (RBS side) cold flue gas is injected at the opposite exhaust wall while near the window bottom surface (COS side) the corresponding atmosphere is recirculated with an alternated scheme. This strategy promotes a significant enhancement of convection heat transfer rates from the window, and consequently, a reduction of its temperature. The thermal conditions and the mechanical stability of the window is of paramount importance for a successful furnace operation. The mechanical failure of the window could lead to a contamination of the COS atmosphere with the corresponding consequences on the burners operation. Additionally, and more dramatically, the mixing between the flue gas (with non-negligible amounts of O_2) and the COS atmosphere (with combustible solvent species) could lead to a catastrophic and fatal failure of the furnace due to the promotion of explosive conditions.

3. Modeling

3.1. Physical models

Figs. 2(a) and 2(b) present the physical 3D and 2D models of the proposed full-scale (entire) furnace. In this work, the 3D full-scale furnace model is considered to investigate the overall thermal and sealing performance of the furnace. The 2D full-scale furnace model is applied to analyze the heating and drying rate of uncoated and coated metal strips. For the 2D full-scale model, the role of the RBS on the COS is emulated through an effective radiative heat source surface – referred to as "radiant wall" – taking into account full-scale furnace performance predictions.

To characterize in detail the processes taking place in the current radiative coil coating furnace concept – in particular, the radiative heating performance for uncoated and coated metal strip samples, as well as the evaporation of solvents from liquid film coatings –, a small-scale (pilot) furnace model was developed in close representativeness
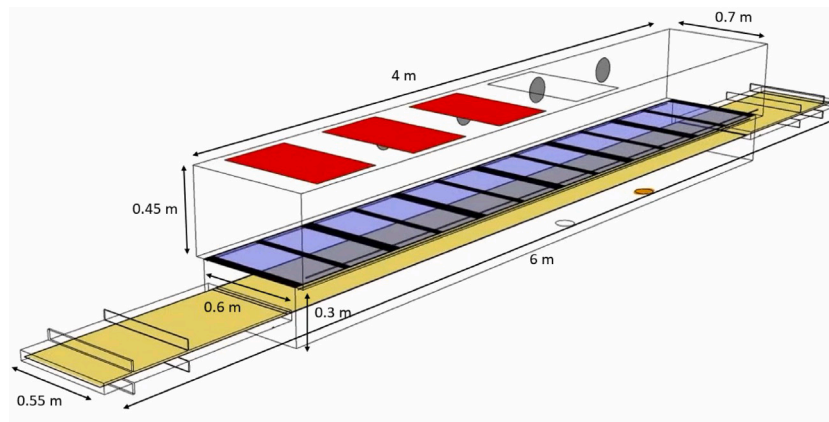
(a)
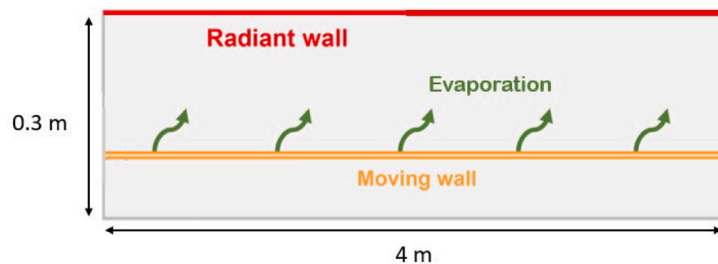
(b)

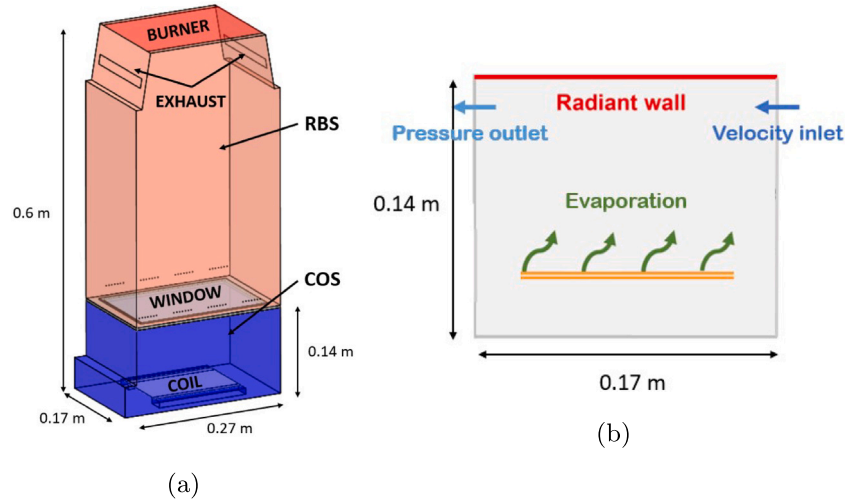**Fig. 2.** Physical 3D (a) and 2D (b) models of the full-scale furnace.

Fig. 3. Physical 3D (a) and 2D (b) models for the small-scale furnace.

of the full-scale furnace model. Figs. 3(a) and 3(b) present the physical 3D and 2D models, respectively, of the small-scale furnace. For the small-scale 3D furnace model, a similar set up was considered (two modules separated by a window partition) but a fixed (motionless) metal sheet sample (coated or uncoated) is placed in the corresponding COS module. (Since the small-scale model operates with a closed COS module, the application of inertization chambers is not required.) As previously for the full-scale 2D model, the role of the RBS on the COS is taken into account through an effective radiative heat source surface (radiant wall). The small-scale 3D model was solely developed to experimentally measure the heating and drying rates of uncoated and coated metallic samples considering a radiant burner unit similar to those applied in each battery of burners considered in the full-scale 3D furnace model (Burners 1 to 4 in Fig. 1).

3.2. Mathematical and numerical models

The mass, momentum, and energy conservation equations written in a time-average formulation and Cartesian tensor notation read as presented in Eqs. (1), (2), (3), respectively.

$$\frac{\partial \rho}{\partial t} + \frac{\partial}{\partial x_i}\left(\rho u_i\right) = S_m \tag{1}$$

$$\frac{\partial}{\partial t}\left(\rho u_i\right) + \frac{\partial}{\partial x_j}\left(\rho u_i u_j\right) = -\frac{\partial p}{\partial x_i} + \frac{\partial}{\partial x_j}\left[\mu\left(\frac{\partial u_i}{\partial x_j} + \frac{\partial u_j}{\partial x_i} - \frac{2}{3}\delta_{ij}\frac{\partial u_i}{\partial x_i}\right)\right] + \frac{\partial}{\partial x_j}\left(-\overline{\rho u_i' u_j'}\right) \tag{2}$$

$$\rho c_p\left[\frac{\partial T}{\partial t} + \frac{\partial}{\partial x_i}\left(u_i T\right)\right] = \frac{\partial}{\partial x_i}\left(\lambda\frac{\partial T}{\partial x_i} - \rho c_p\overline{u_i' T'}\right) \tag{3}$$

In these equations, u_i is the fluid velocity and the index $i = 1, 2, 3$ refers to the x-, y-, and z-direction. Additionally, ρ, p, μ, T, and λ correspond to the fluid density, static pressure, dynamic viscosity, temperature, and thermal conductivity, respectively. The Reynolds stresses $(-\overline{\rho u_i' u_j'})$ and turbulent heat flux $(\overline{u_i' T'})$ are modeled according to the selected turbulence model. Moreover, the transport equation for scalar variables is given by Eq. (4), where ϕ corresponds to the species mass fractions and the turbulence model variables, and $\Gamma_{\phi,\text{eff}}$ and S_ϕ are the effective diffusion coefficient and the source term, respectively, of the corresponding equation.

$$\frac{\partial}{\partial t}\left(\rho\phi\right) + \frac{\partial}{\partial x_i}\left(\rho u_i\phi - \Gamma_{\phi,\text{eff}}\frac{\partial\phi}{\partial x_i}\right) = S_\phi \tag{4}$$

The ideal gas model is considered for the evaluation of the fluid density. The realizable $k - \varepsilon$ turbulence model [20] with standard WF is applied to provide closure for the RANS equations, in line with Ref. [17]. The realizable $k - \varepsilon$ model is an improvement over the standard $k - \varepsilon$ since it uses a modified transport equation for the dissipation rate and includes an alternative formulation for the turbulent viscosity. This transport equation was developed from an exact equation for mean-square vorticity fluctuation transport.

According to the realizable $k - \varepsilon$ model, the transport equations for k (turbulent kinetic energy) and ε (turbulent dissipation rate) are given by Eqs. (5) and (6), respectively. Note that the k governing equation is the same for the standard $k - \varepsilon$ model equation, except for the model constants. In Eqs. (5) and (6), G_k and G_b stand for the generation of turbulence kinetic energy by mean velocity gradients and buoyancy, respectively, Y_M corresponds to the contribution of the fluctuating dilatation, while σ_k and σ_ε are the k and ε, respectively, turbulent Prandtl numbers. The C variables are constants and the S variables are source terms.

$$\frac{\partial}{\partial t}\left(\rho k\right) + \frac{\partial}{\partial x_j}\left(\rho k u_j\right) = \frac{\partial}{\partial x_j}\left[\left(\mu + \frac{\mu_t}{\sigma_k}\right)\frac{\partial k}{\partial x_j}\right] + G_k + G_b - \rho\varepsilon - Y_M + S_k \tag{5}$$

$$\frac{\partial}{\partial t}\left(\rho\varepsilon\right) + \frac{\partial}{\partial x_j}\left(\rho\varepsilon u_j\right) = \frac{\partial}{\partial x_j}\left[\left(\mu + \frac{\mu_t}{\sigma_\varepsilon}\right)\frac{\partial\varepsilon}{\partial x_j}\right] + \rho C_1 S\varepsilon - \rho C_2\frac{\varepsilon^2}{k + \sqrt{v\varepsilon}} + C_{1\varepsilon}\frac{\varepsilon}{k}C_{3\varepsilon}G_b + S_\varepsilon \tag{6}$$

The discrete ordinates (DO) model was considered to evaluate the radiative heat transfer contribution to the energy balance equations of gas and solid regions. This model determines the net radiative heat flux at the surfaces of the oven – as the net radiation model (commonly known as the surface-to-surface model) does – but, most importantly, the net volumetric radiative energy source due to absorption and emission (and, eventually, scattering) within the volume of participating media. The window material is considered as a participating medium for radiative heat transfer purposes — the window material simultaneously absorbs and emits radiation. The DO radiation model relies on a pre-defined angular discretization scheme which effects simultaneously the solution accuracy and the computational cost.

The fluid was defined as a multi-component gas mixture comprising O_2, H_2O, CO_2, N_2, and a representative solvent species. The viscosity of each species was based on Sutherland's law, the specific heat is a function of temperature and is related by the piecewise-polynomial function, and the thermal conductivity was calculated according to the kinetic theory. In the full-scale 3D furnace mathematical model

(Eqs. (1)–(6) solved for steady-state conditions), the evaporation of the solvent is taken into account through a uniform volume mass source above the metal strip, computed based on the current operating condition and on the properties of the representative solvent species. In this work, 1,3,5-Trimethyl-benzene is considered the representative solvent species corresponding to the application of PU coating. The main properties of this species were gathered from NIST database [21].

In the full- and small-scale 2D furnace models, the transient form of Eqs. (1)–(6) is considered and the evaporation of the solvent is taken into account through the Eulerian wall film model (EWF). This model solves mass, momentum, and heat transfer for the film, assuming that the film flows always parallel to the surface (the normal component of the film velocity is zero) – see Eqs. (7)–(9).

$$\frac{\partial \rho_l h}{\partial t} + \nabla_s \cdot \left(\rho_l h \vec{V}_l \right) = \dot{m}_s \tag{7}$$

$$\frac{\partial \rho_l h \vec{V}_l}{\partial t} + \nabla_s \cdot \left(\rho_l h \vec{V}_l \vec{V}_l + \vec{D}_V \right) = -h \nabla_s P_L + \rho_l h \vec{g}_\tau + \frac{3}{2} \vec{\tau}_{fs} - \frac{3\mu_l}{h} \vec{V}_l + \vec{\tau}_{\theta_w} \tag{8}$$

$$\frac{\partial \rho_l h T_f}{\partial t} + \nabla_s \cdot \left(\rho_l h T_f \vec{V}_l + \vec{D}_T \right) = \frac{1}{c_p} \left[\frac{2\lambda_f}{h} \left(T_s + T_w - 2T_m \right) + \dot{m}_{vap} L \right] \tag{9}$$

In Eq. (7), ρ_l, h, ∇_s, $\vec{V}_l$, and $\dot{m}_s$ correspond to the liquid density, film height, surface gradient operator, mean film velocity, and mass source per unit wall area due to phase change, respectively. In Eq. (8), the terms on the left hand side represent transient and convection effects and $\vec{D}_V$ corresponds to the tensor denoting the differential advection term — computed based on the quadratic film velocity profile. On the right hand side, it is represented the effects of gas-flow pressure, gravity in the direction parallel to the film, viscous shear force on the gas–film and film–wall interfaces, and surface force due to film liquid surface tension. In Eq. (9), T_f, T_s, T_W, and T_m are the average film temperature, film surface temperature, wall temperature, and film half depth temperature. On the right hand side, it is represented the net heat flux on the gas–film and film–wall interfaces, $\dot{m}_{vap}$ is the mass vaporization rate, and L is the latent heat associated with the phase change.

Additionally, to consider the phase changes between the film and gas species, the Eulerian wall film model is coupled with the mixture species transport model. This phase change is suitable for problems where the vapor is mixed with non-condensable gases (e.g. solvent and air). The phase change rate is modeled through the diffusion balance model given by Eq. (10).

$$\dot{m}_{phase} = \frac{(\rho D/\delta)}{\rho D/\delta + C_{phase}} C_{phase} \left(\phi_{sat} - \phi_i \right) \tag{10}$$

In this equation, ρ, D, δ, C_{phase}, and ϕ_i are the gas mixture density, vapor species diffusivity, cell-center-to-wall distance, phase change constant, and cell-center mass fraction of the vapor species, respectively.

The problem governing equations were numerically solved in FLUENT (version 16.2). The convection and diffusion terms were discretized using second-order schemes and an implicit temporal discretization scheme was used. The SIMPLE algorithm was considered for the pressure–velocity coupling. At each time step, the solutions were assumed to be converged when residuals of all the equations decreased three orders of magnitude. More details of these models and corresponding numerical implementation can be found in Ref. [22].

3.3. Boundary conditions

In the full-scale 3D furnace numerical simulations, the COS and RBS simulations were performed together, and the energy exchange occurs through the window. The boundary conditions related to the solvent species evaporation were prescribed as a mass source with a certain value according to the operation condition, defined along the metal strip inside the COS. The injection of solvent from the moving metal strip can be characterized by a certain velocity according to the operation condition and with a temperature imposed at the interface with the fluid region. This temperature imposed was constant at the pre-inertization chamber zone (300 K) and with a linear increase inside the COS from 300 K to 526 K, where the temperature was then kept constant in the post-inertization chamber. In the pre- and post-inertization chambers, there are the injection and extraction systems to avoid the external oxygen entrance to the COS and solvent leakage from the COS. At the injection inlet section, according to the operation condition, a particular mass flow rate was specified with a certain molar composition. While at the extraction (outlet) section, a certain pressure outlet with a target mass flow rate was defined. After the converged solution is achieved, the mass flow rate value was verified and was in accordance with the target value. The open boundary sections at the inlet and exit of the system were of extreme importance for the enclosure of the system. These zones were defined as open boundaries in which the environment atmospheric pressure was prescribed, and the flow is free to enter or leave the system. Inside the curing oven section, two sub-systems are present. The extraction system – which aims to collect the evaporated solvent species – is located at the bottom of the section and it was defined with a specific mass flow rate leaving the system, which can change with the operation condition. The remaining system was the recirculation system which promotes the recirculation of the flow inside the COS. Particular mass flow rate and temperature values are considered at the inlet sections of the recirculation system.

The operating conditions considered for the full-scale 3D numerical simulations – required for defining the corresponding boundary conditions – are listed in Table 1, for three different cases: (i) minimal; (ii) nominal; and (iii) maximal.

Concerning the 2D numerical simulations, only the COS is resolved in full detail. The RBS effect is emulated in the COS performance through an effective radiative heat source surface for which a particular temperature profile – depending on the case under consideration – is defined, in such a way that the role of the RBS (and the window) is included.

3.4. Computational mesh details

The 3D computational domains were discretized considering hexahedron cells as depicted in Fig. 4. This mesh type was chosen because the model geometry follows three perpendicular directions as axes (x, y, and z). Also, even though the flow is 3D, the injected fluid stream's principal direction is also aligned with these axes, decreasing numerical false diffusion, and improving accuracy. Because of its simplicity, and especially in terms of precision, this type of cell provides advantages. This discretization is crucial, not just in terms of accuracy, but also in terms of the computational effort required to reach a convergent solution.

Aside from cell type, the size of the cell base is also essential. This value reflects a trade-off between precision and computational cost. As a result, the cell size should be as small (large) as feasible to improve accuracy (decrease the computational burden). Local refinement was applied instead of using a uniform cell base size over the whole computational domain in order to achieve highly resolved solution fields in selected locations — regions where the solution variables display large spatial changes. For example, the zones near the metal strip are very refined so as the region between the window and the cooling gas injection slots above the window. Overall, the total number of cells in the 3D model is approximately 7.4 millions.

For the full- and small-scale 2D furnace simulations, the corresponding meshes were developed in accordance with the 3D mesh procedure. The meshes are non-uniform with refinements close to the metal strip and injection slot.

Table 1

Operating conditions considered for the minimal, nominal, and maximal cases. (IC — inertization chambers.).

| Region	Parameter	Operating condition		
		Minimal	Nominal	Maximal
RBS	Active batteries of burners	1 to 2	1 to 3	1 to 4
	Power per active battery of burners [kW]	40	200	200
	Total flue gas mass flow rate [kg/s]	0.022365	0.1117	0.11138
	Flue gas composition			
	H_2O mole fraction [–]	0.128	0.135	0.137
	CO_2 mole fraction [–]	0.099	0.097	0.091
	O_2 mole fraction [–]	0.039	0.036	0.039
	N_2 mole fraction [–]		to balance	
	Flue gas temperature [K]	1485.24	1507.32	1489.09
	Burners effective surface temperature [K]	1000	1673	1673
	Total cooling gas mass flow rate [kg/s]	0.037785	0.049790	0.074959
	Cooling gas injection temperature [K]	353.15	353.15	353.15
COS	Total extracted COS gas mass flow rate [kg/s]	0.011653	0.085536	0.111627
	Tot. atmos. recirculation mass flow rate [kg/s]	0.00793	0.00793	0.00759
	Recirculation gas inlet temperate [K]	523.01	562.98	630.24
IC	Total injected flue gas mass flow rate [kg/s]	0.011182	0.083756	0.111385
	Injected flue gas inlet temperature [K]	359.38	359.44	359.50
	Total extracted flue gas mass flow rate [kg/s]	0.013582	0.100500	0.133668
Coil	Metal strip velocity [m/s]	0.083	0.500	0.500
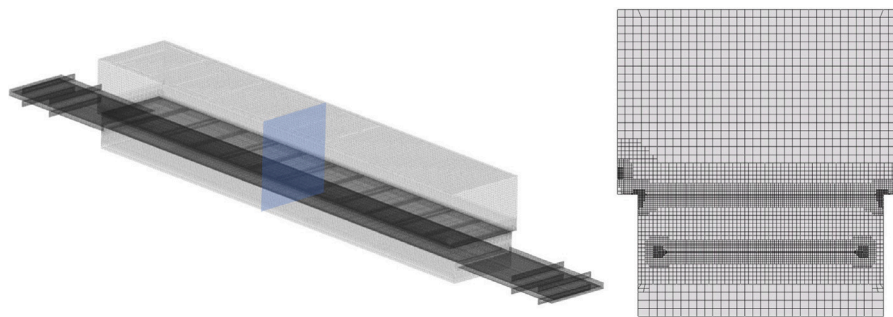
Fig. 4. Representation of the mesh considered for the full-scale 3D numerical simulations. The right inset corresponds to the mesh for the highlighted furnace transversal plane.

4. Results and discussion

Full-scale 3D furnace numerical simulations results obtained under steady-state conditions are presented in Section 4.1 to investigate the overall thermal engineering performance and safety requirements of the curing furnace. Afterwards, small- and full-scale 2D furnace numerical simulation results are presented to analyze in detail the process of heating and drying of uncoated and coated metal sheets (Section 4.2). In the later section, the evaporation of solvents from liquid film coatings is addressed.

4.1. Full-scale furnace thermal and shielding performance

To ensure a successful oven operation, the following issues require a particular in-depth investigation: (i) window thermal performance; (ii) inertization chambers effectiveness; and (iii) radiative power available for drying and curing processes. These topics are properly addressed in the sections that follow — Sections 4.1.1–4.1.3.

4.1.1. Window and RBS thermal performance

Figs. 5(a), 5(b), and 5(c) present the temperature distribution of the window top surface for the three operating conditions under consideration — see Table 1. Figs. 5(a) to 5(c) also present the metal frame that holds the glass window in place — higher temperature regions particularly noticeable in Figs. 5(b) and 5(c). Regardless of the operating condition under consideration, the higher temperature regions are registered underneath the active batteries of burners due to the flue gas jet impingement on the window top surface and to the window net radiative heat absorption — the later contribution is more relevant for the nominal and maximal operating conditions for which the burners effective surface temperature is equal to 1673 K (see Table 1). For each operating condition, lower temperatures are observed near the cooling gas injection sections — this evidence is most striking for the minimal operating condition (see Fig. 5(a)).

The net radiative power from the active batteries of burners accounts for 24.79 kW, 182.02 kW, and 242.63 kW for the minimal, nominal, and maximal operating conditions, respectively. These values correspond to an overall porous burners radiative efficiency of about 30.98%, 30.34%, and 30.33% for the minimal, nominal, and maximal operating conditions, respectively. (These values are well within the typical radiative efficiency range reported in the literature for radiant porous burners applications [23–25].) The window absorbs a fraction of the burners radiative energy and the power removed from the window corresponds to 5.47 kW (minimal case), 26.64 kW (nominal case), and 34.81 kW (maximal case). Without the cooling gas application at the RBS environment and for the nominal case, the power removed from the window is equal to 9.13 kW. For this operating condition, the application of the cooling gas at the RBS promotes a decrease of the average window temperature by about 164 K.

Figs. 6(a)–(b), 7(a)–(b), and 8(a)–(b) present streamlines in the RBS with the local temperature values for the minimal, nominal, and maximal operating conditions, respectively. Figs. 6(a), 7(a), and 8(a) are related with the injected cooling gas whereas Figs. 6(b), 7(b), and 8(b) include contributions from the cooling gas and the burners flue gas at four different RBS transversal planes. For all operating conditions, the attachment of the cooling gas flow to the window top surface is observed, which gives confidence to the function of the cooling system in reducing window temperature, leading to a uniform field of temperature.
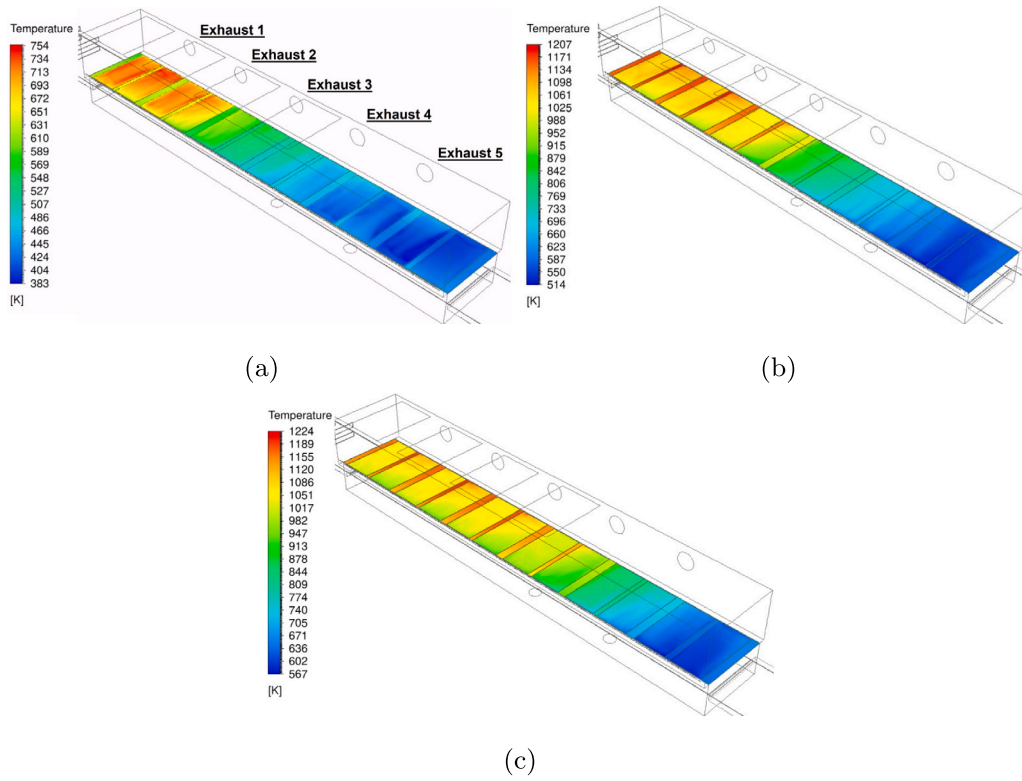
Fig. 5. Window (top surface) temperature distribution for different furnace operating conditions: (a) minimal case; (b) nominal case; and (c) maximal case.
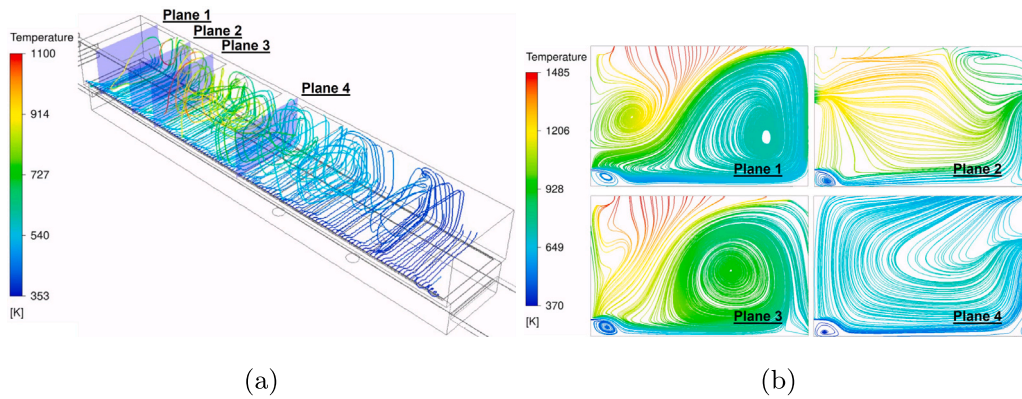

Fig. 6. Streamlines with the corresponding local temperature values in the RBS for the minimum operating condition: (a) injected cooling gas; and (b) injected cooling gas and burners flue gas in four different transversal planes.
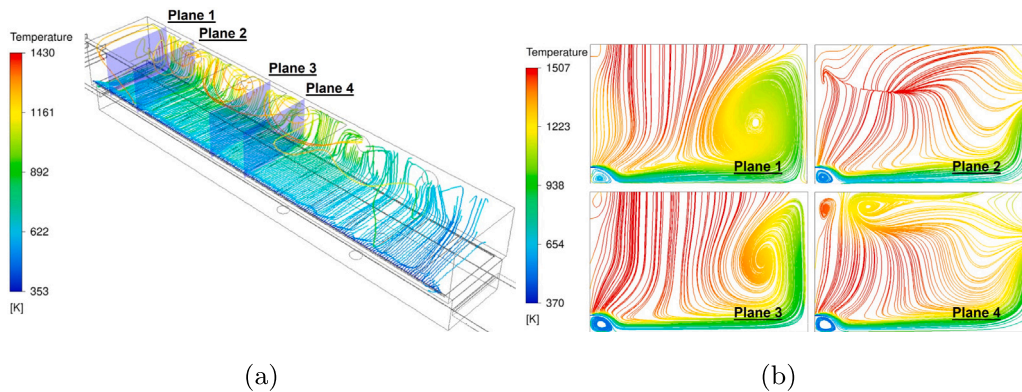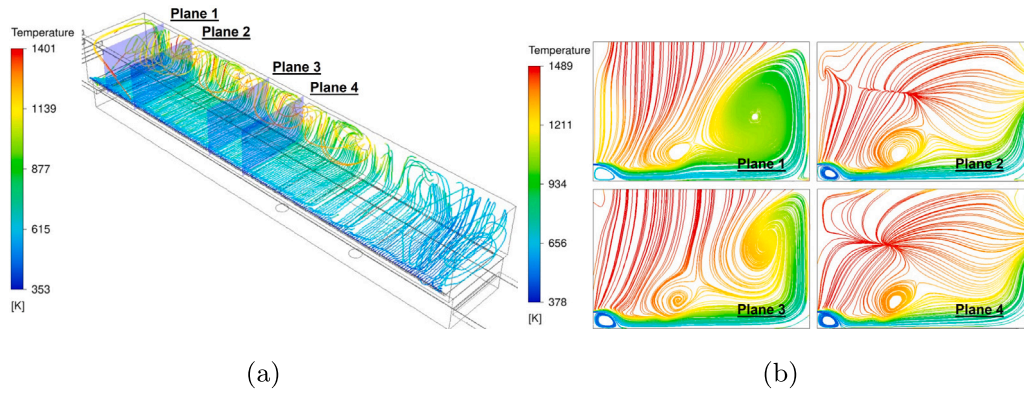

Fig. 7. Streamlines with the corresponding local temperature values in the RBS for the nominal operating condition: (a) injected cooling gas; and (b) injected cooling gas and burners flue gas in four different transversal planes.

(a)

(b)

Fig. 8. Streamlines with the corresponding local temperature values in the RBS for the maximal operating condition: (a) injected cooling gas; and (b) injected cooling gas and burners flue gas in four different transversal planes.
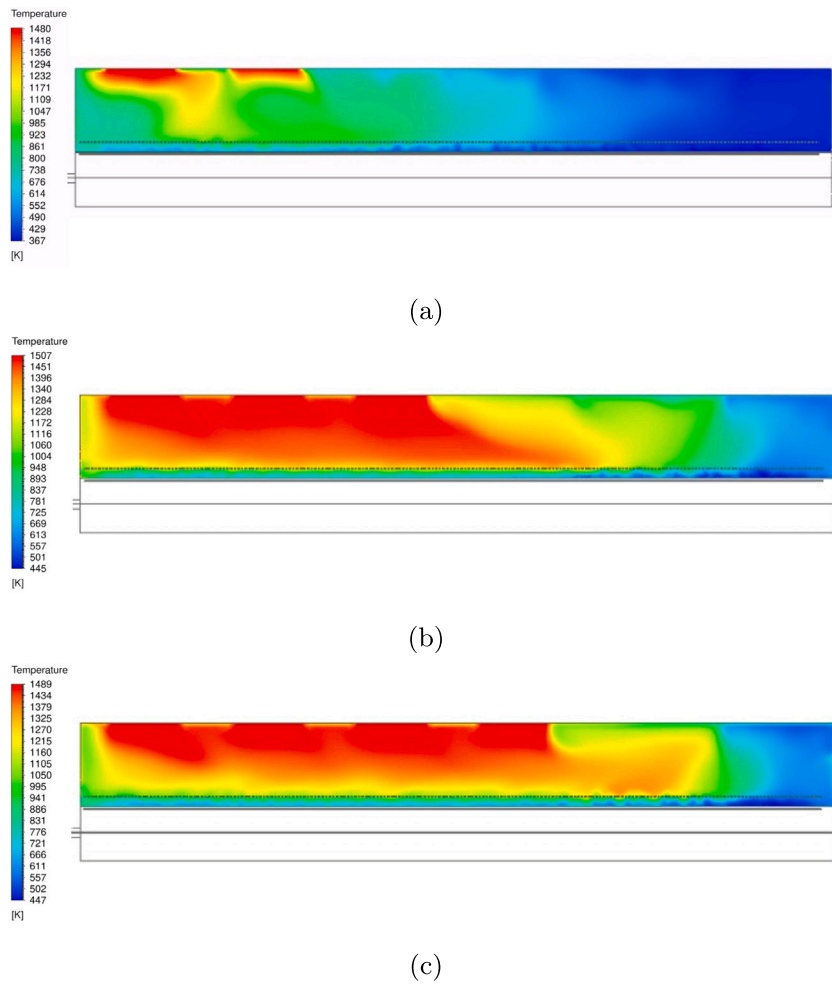

(a)

(b)

(c)

Fig. 9. Temperature distribution at the RBS longitudinal mid-plane for different furnace operating conditions: (a) minimal case; (b) nominal case; and (c) maximal case.

Table 2 lists the average temperature of the window, flue gas (RBS fluid), and RBS walls for the three furnace operating conditions under consideration. In addition, Figs. 9(a)–(c) present the temperature distribution at the RBS mid-plane section for the three operation conditions. The highest average temperatures for the window, flue gas, and RBS walls are observed for the maximal operating condition — see Table 2. Figs. 9(a)–(c) show that significantly lower fluid temperatures are observed just above the window due to the injection of cooling gas. In particular, for the minimal operating condition, the flue gas temperatures are strikingly lower than the flue gas temperatures for

the remaining operating conditions, since only the first two batteries of burners are active and a significant cooling gas mass flow rate is applied (see Table 1).

Finally, the average velocity, average temperature, and mass flow rate at each RBS exhaust section (see Fig. 5(a) to locate each exhaust section) are presented in Table 3. Due to its location, Exhaust 1 removes flue gas at the highest average temperatures, independently of the operating condition. However, exhaust sections located far from active batteries of burners remove, in general, a higher amount of flue gas per unit time. The resulting exhaust fluid mixture temperature (obtained
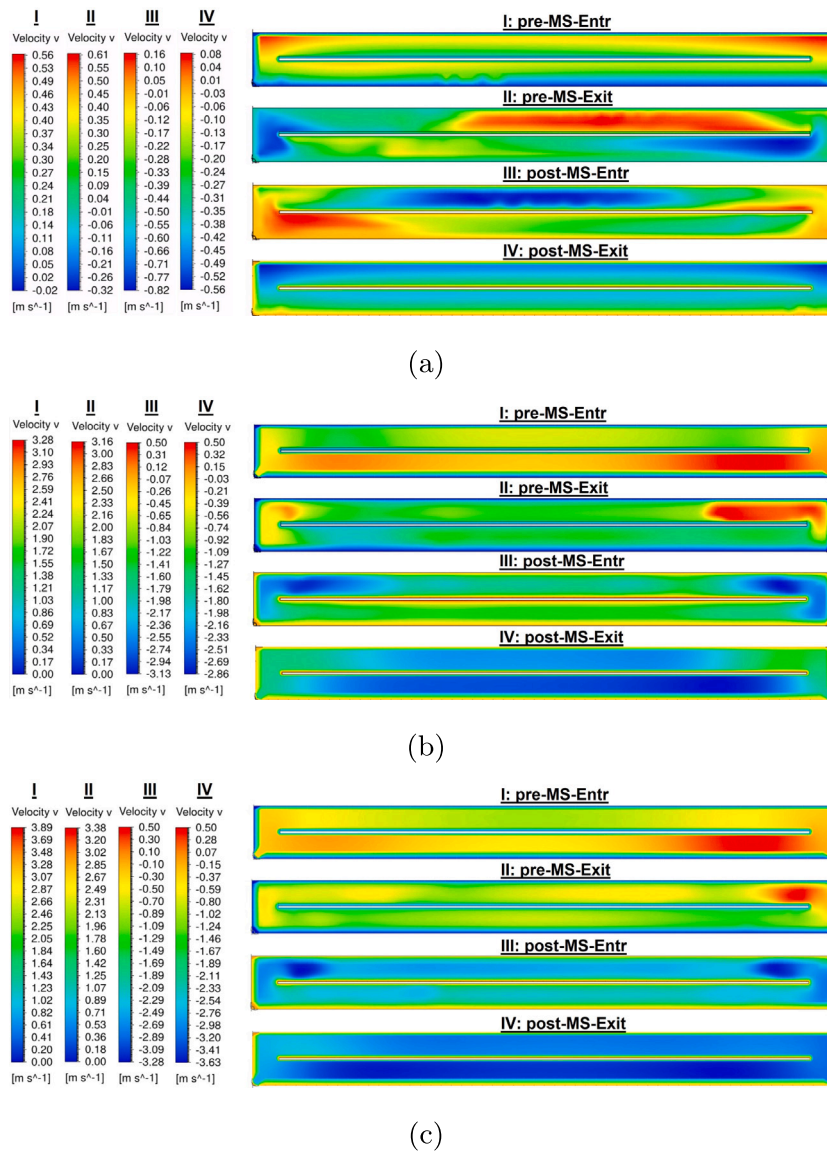
Fig. 10. Velocity distribution (velocity component aligned with the metal strip moving direction) at different furnace transversal planes of the pre- and post-inertization chambers and for different operating conditions: (a) minimal case; (b) nominal case; and (c) maximal case. The planes labeled as "pre-MS-Entr" and "pre-MS-Exit" correspond to the planes (interfaces) located between the pre-IC and the surrounding (external) air and between the pre-IC and the COS, respectively. The planes labeled as "post-MS-Entr" and "post-MS-Exit" correspond to the planes (interfaces) located between the COS and post-IC and between the post-IC and surrounding (external) air, respectively.

Table 2
Average temperature for different regions and for the minimal, nominal, and maximal operating conditions.

Region	Average temperature [K]		
	Minimal	Nominal	Maximal
Window	547.71	866.14	932.79
RBS – Fluid	684.20	1128.68	1129.39
RBS – Walls	608.35	1043.00	1149.11

considering the weighted average) is equal to 585, 1009, and 998 K for the minimal, nominal, and maximal operating conditions, respectively.

4.1.2. COS safety and sealing proof

Each inertization chamber (IC) consists of a channel crossed by the metal strip with two flue gas injection sections and two extraction sections — both injection and extraction are performed from the channel top and bottom surfaces (see Fig. 1). The main purpose of

the inertization chambers is to provide shielding for the COS atmosphere. Figs. 10(a), (b), and (c) present for the minimal, nominal, and maximal operating conditions, respectively, the distribution of the velocity component aligned with the metal strip moving direction at different furnace transversal planes of the pre-IC and post-IC. For the maximal and nominal operating conditions, no reversed flow is observed in the pre-IC sections (sections "pre-MS-Entr" and "pre-MS-Exit") while a negligible reversed flow condition near the coil in the post-IC sections ("post-MS-Entr" and "post-MS-Exit") is registered due to coil movement. However, for the minimal operating condition, a negligible reversed flow is noticed at the metal strip entrance section in the pre-IC and at the metal strip exit section of the post-IC. For this operating condition, reversed flow features are also observed at the interfaces of inertization chambers with the COS (sections "pre-MS-Exit" and "post-MS-Entr"), being this operating condition the more susceptible to failure concerning the COS atmosphere shielding.

For the minimal operating condition, Figs. 11(a) and 11(b) present contours of O_2 mass fraction in three longitudinal planes of the pre-IC and post-IC, and Figs. 11(c) and 11(d) present contours of solvent
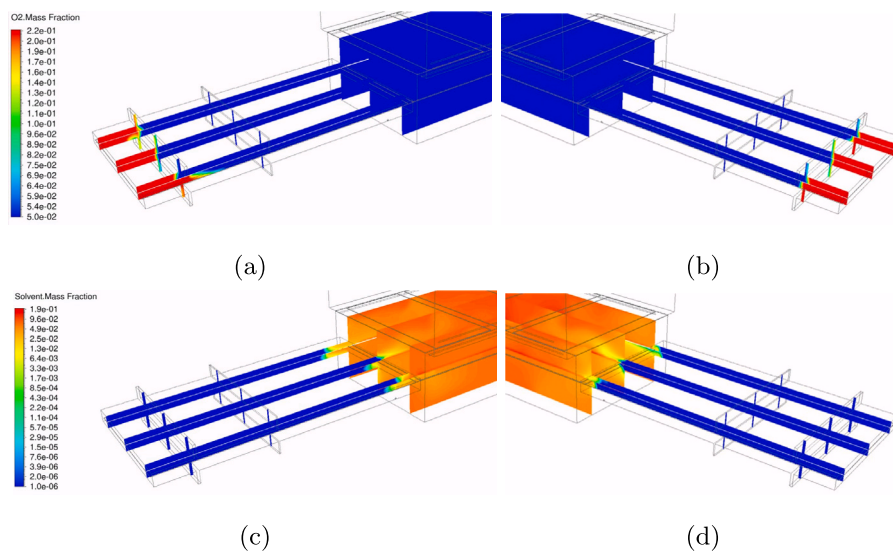
Fig. 11. O_2 mass fraction distribution ((a) and (b)) and solvent mass fraction distribution ((c) e (d)) at three cross-sectional planes in the pre-inertization ((a) and (c)) and post-inertization ((b) and (d)) chambers.
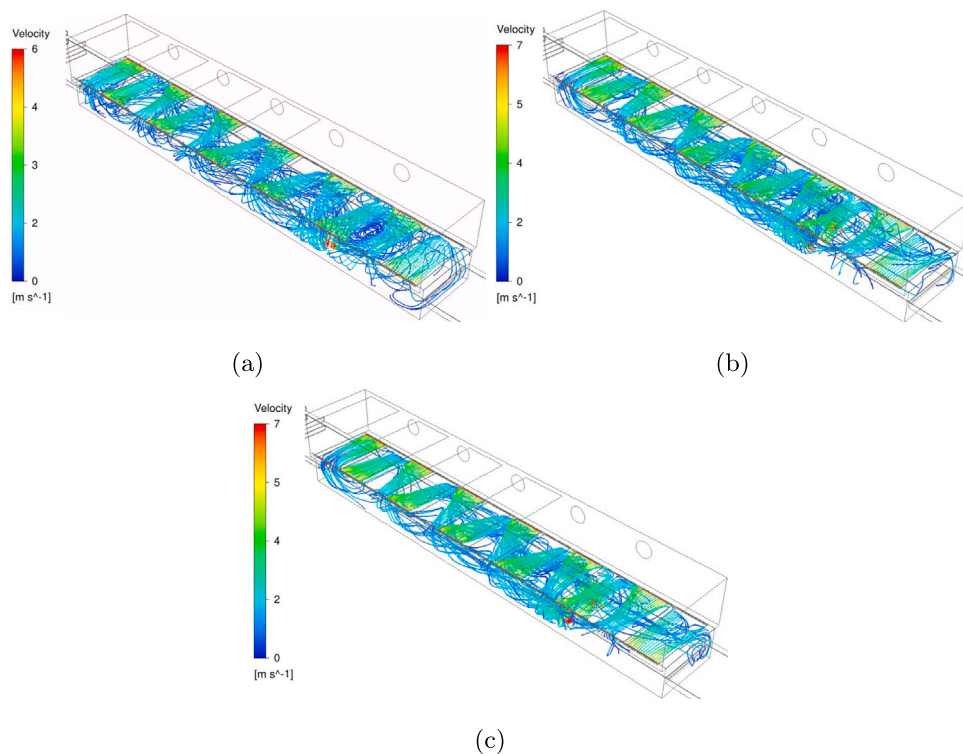

Fig. 12. COS Streamlines for different operating conditions: (a) minimal case; (b) nominal case; and (c) maximal case.

Table 3
Average velocity, average temperature, and mass flow rate at each RBS exhaust section for the minimal (Min.), nominal (Nom.), and maximal (Max.) operating conditions. (The location of each RBS exhaust section can be found in Fig. 5(a).)

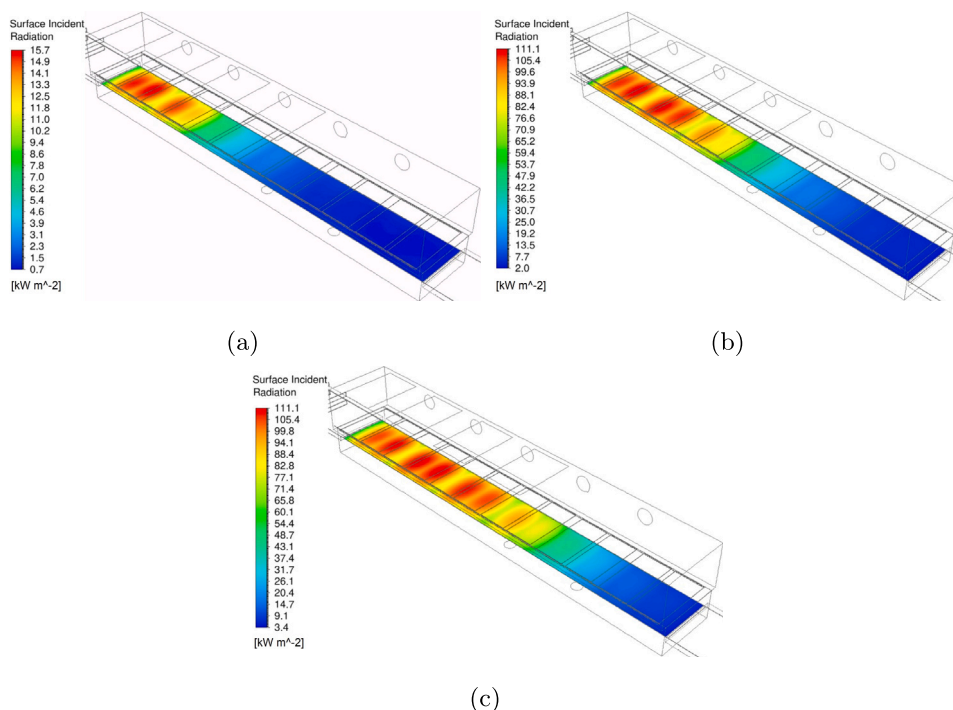| Exhaust	Avg. velocity [m/s]			Avg. temperature [K]			Mass flow rate [kg/s]		
	Min.	Nom.	Max.	Min.	Nom.	Max.	Min.	Nom.	Max.
1	7.96	26.47	34.41	808.37	1142.82	1074.18	0.04820	0.1245	0.1721
2	7.73	26.59	34.79	745.00	1141.08	1091.36	0.05174	0.1247	0.1711
3	6.90	25.75	34.56	596.06	1088.24	1084.17	0.05693	0.1264	0.1724
4	6.27	24.70	33.00	476.08	992.15	996.79	0.06341	0.1330	0.1782
5	5.87	21.49	29.49	397.74	742.68	779.78	0.06896	0.1536	0.2016

Fig. 13. Coil incident radiation for different operating conditions: (a) minimal case; (b) nominal case; and (c) maximal case.

mass fraction in the same planes. No solvent leakage to the environment is observed, leading to the conclusion that the jets in the inertization chambers block the small amount of solvent exiting the COS. At the same time, the inertization jets prevent oxygen from the surrounding environment to reach the COS by being removed by the exhaust stream. This is also observed due to a higher mass flow rate at the extraction than at the injection, allowing the inertization process to ensure a safe operation for all cases.

Moreover, Figs. 12(a), (b), and (c) show the streamlines inside the COS for the injected cooling gas (COS gas mixture recirculation) for the minimal, nominal, and maximal operating conditions, respectively. (The COS gas mixture recirculation has three main purposes: (i) remove heat from the window; (ii) promote high solvent transport rates from the coating top surface; and (iii) promote a uniform mixture composition throughout the oven.) It is possible to verify that the recirculation scheme below the window is alternated, for all the cases. Finally, it is important to highlight that the average temperature inside the COS is equal to 478.17 K, 510.32 K, and 520.91 K for the minimal, nominal, and maximal operating conditions, respectively.

4.1.3. Coil surface irradiation and overall furnace energy balance

Figs. 13(a), 13(b), and 13(c) show contours of the coil incident radiation for the minimal, nominal, and maximal operating conditions, respectively. Regardless of the operating condition under consideration, the regions with higher incident radiation are registered underneath the active batteries of burners. The radiative power absorbed in the coil is proportional to the operating condition under consideration, corresponding to about 13.76 kW (minimal case), 113.60 kW (nominal case), and 150.06 kW (maximal case). Hence, the coil absorbs 55.53%, 62.40%, and 61.85% of the total burners' radiative power for the minimal, nominal, and maximal operating conditions, respectively. These values are in full compliance with the minimum of 55% established.

Table 4 presents the fraction of the total power provided by the burners that is absorbed by the coil, COS walls, RBS walls, and window for the three operating conditions under consideration. The net radiative heat transfer rate absorbed by the walls is transferred by convection to the surrounding fluid — heat losses through the walls

Table 4
Ratio between the absorbed power and the total burners' radiative power for each region considering the minimal, nominal, and maximal operating conditions.

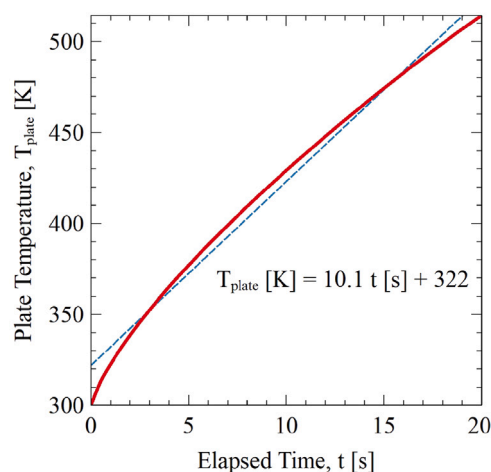| Region	Relative absorbed power [%]		
	Minimal	Nominal	Maximal
Coil	55.53	62.40	61.85
COS walls	1.05	7.27	4.73
RBS walls	21.35	15.70	19.07
Window	22.07	14.63	14.35

Fig. 14. Plate temperature profile for a radiant wall temperature equal to 846 K, without recirculation and film evaporation.

are negligible due to the insulation conditions. Therefore, a significant fraction of the net radiative power provided by the burners is carried away from the furnace by the flue gas — the fraction corresponding to the RBS walls. Moreover, to keep the window as cold as possible a large fraction of power is removed from the window — up to about 22% for the minimal operating condition.

4.2. Heating and drying performance

4.2.1. Small-scale furnace

A small-scale model furnace was manufactured (see Fig. 3) to investigate the unsteady drying and curing processes of paint-coated metal sheets under IR radiation. The experimental program first characterized the unsteady plate heating rate and then the film evaporation. An unsteady 2D model of the small-scale oven was developed to compare numerical predictions with experimental results. The simulations were performed considering only the COS with an effective radiative heat source surface (radiant wall) as the top surface. The influence of several parameters was studied, such as the radiant wall temperature, film thickness, and surface plate emissivity.

Heating experiments of the plate (coil) were performed by inserting a plate at $t = 0$ near the bottom of the model oven. Consequently, the transient simulations were conducted considering as initial condition the result of a steady-state simulation of the COS and at $t = 0$ a particular initial plate temperature was prescribed. Thermal losses through the walls were imposed by an overall heat transfer coefficient computed considering the wall material and thickness and the surrounding environment (ranging from 1.65 to 19.74 W/m² K, depending on the considered wall). In addition, when considering film evaporation, a certain air flow rate at ambient temperature was imposed (to promote atmosphere recirculation) at one side (2.75 kg/m² s).

Firstly, to validate the model, a transient study of the plate temperature was conducted for an experimentally evaluated radiant wall temperature of 846 K, without recirculation or liquid film (coating) application. Fig. 14 shows the temporal variation of the spatially-averaged plate temperature during the first 20 s. The calculated temporal temperature profile results in an average plate heating rate equal to 10.1 K/s which is close to the value measured experimentally (9.5 K/s) under similar conditions.

Parametric studies were conducted to investigate the influence of the radiant wall temperature, initial film thickness, and surface emissivity on the temporal profiles of the plate temperature, film thickness, and solvent mass fraction at the extraction section. Figs. 15(a), (b), and (c) present the effect of the radiant wall temperature on the plate temperature, film thickness, and solvent mass fraction at the extraction, respectively. Three radiant wall temperatures were considered – 750, 770, and 790 K –, while the initial film thickness and surface (coating/plate) emissivity were kept constant and equal to 40 μm and 0.67, respectively. Fig. 15(a) shows that for each radiant wall temperature the addition of the film lowers the heating rate of the plate since part of the energy that would be applied to heat the plate is used to evaporate the film. Additionally, it is worth mentioning that there is a radiant wall temperature that induces a plate heating rate very similar to the experimental one. Moreover, Fig. 15(b) shows that the increase of the radiant wall temperature promotes a faster film evaporation. The
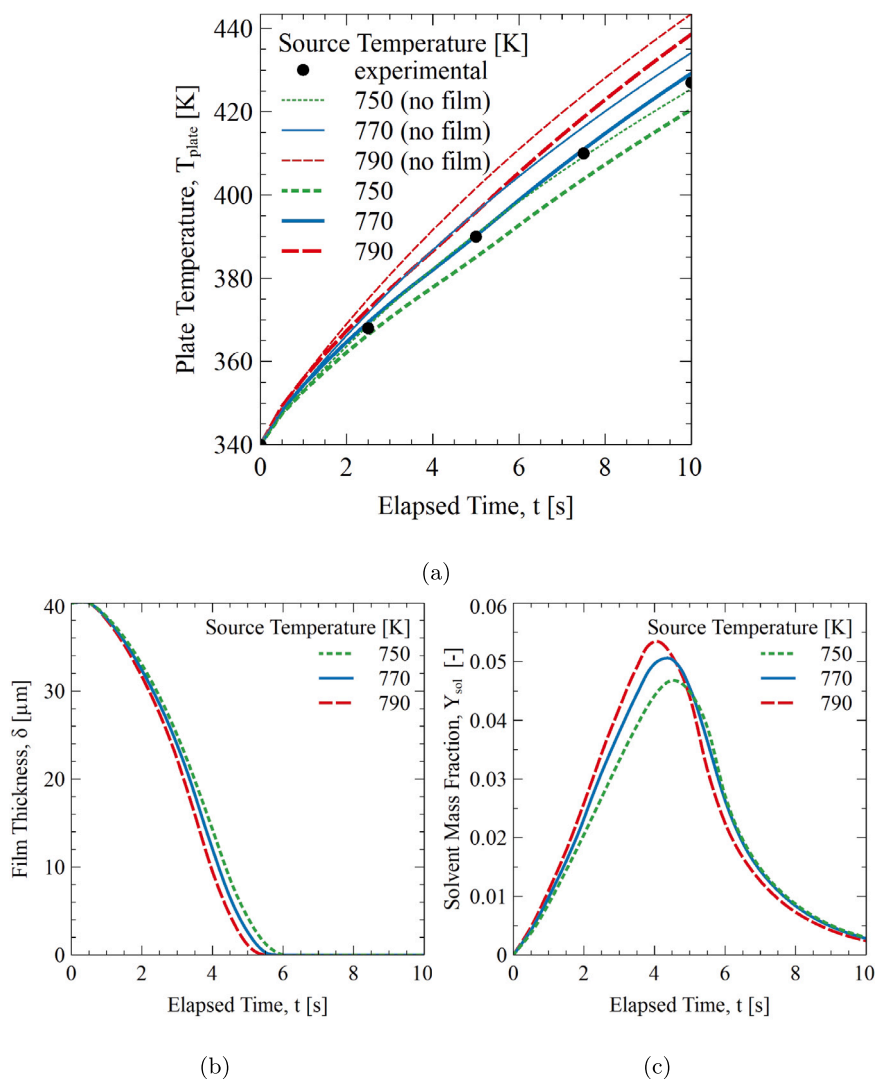

(a)

(b)   (c)

Fig. 15. Radiant wall temperature influence on the plate temperature (a), film thickness (b), and solvent mass fraction at the extraction section (c).

profile of the solvent mass fraction at the extraction section (Fig. 15(c)) has a behavior compatible with the profile of the film thickness. When the required time to completely evaporate the film is reduced – *i.e.*, increasing the radiant wall temperature –, the elapsed time to observe the peak on the profile of the solvent mass fraction at the extraction section is also reduced (see Fig. 15(c)).

Figs. 16(a), (b), and (c) present the effect of the initial film thickness on the plate temperature, film thickness, and solvent mass fraction at the extraction, respectively. Three initial film thickness values were considered – 20, 40, and 60 μm –, while the radiant wall temperature and surface emissivity were kept constant and equal to 770 K and 0.67, respectively. Fig. 16(a) shows that an increase of the initial film thickness leads to a slight reduction on the plate heating rate due to an increase in the heat transfer resistance. In addition, the thicker the film is, the longer it takes to completely evaporate it (Fig. 16(b)), and the longer it takes to observe the peak in the solvent mass fraction profile at the extraction section (Fig. 16(c)). Moreover, since the only difference between the simulations is the initial film thickness, the slopes of the mass fraction are identical due to the similar heating rate. Thus, it is expected that the evaporation rate is the same for different initial film thicknesses.

Figs. 17(a), (b), and (c) present the effect of the surface emissivity on the plate temperature, film thickness, and solvent mass fraction at the extraction, respectively. Three different surface emissivity values

were considered — 0.57, 0.67, and 0.77 –, while the radiant wall temperature and initial film thickness were kept constant and equal to 770 K and 40 μm, respectively. Fig. 17(a) shows that an increase in the surface emissivity induces an increase on the plate heating rate, and consequently, reduces the required time to observe the complete film evaporation (see Fig. 17(b)), and the peak on the solvent mass fraction profile at the extraction section (see Fig. 17(c)).

4.2.2. Full-scale furnace

To simulate the performance of film evaporation in the full-scale oven, a similar simulation to the previous one was conducted. The geometry was modified, recirculation in the COS was not considered, and a uniform effective radiative heat source temperature (1100 K) was imposed to attain the equivalent coil absorbed radiation of the nominal 3D model results — see the corresponding geometry in Fig. 2(b).

Firstly, it was simulated the heating of the coil for the mentioned conditions. This simulation was conducted through a piecewise constant reconstruction, by updating the temperature profile of the coil after a certain number of time steps, considering that the coil is entering at 300 K. Since the incident radiation was considered constant along the length of the oven, a linear temperature profile from 300 K to 526 K was obtained. This result is in full agreement with the prescribed temperature profile in the 3D model simulations.

Afterwards, the computed temperature profile was imposed and a zone for the film injection was created above the metal strip since the
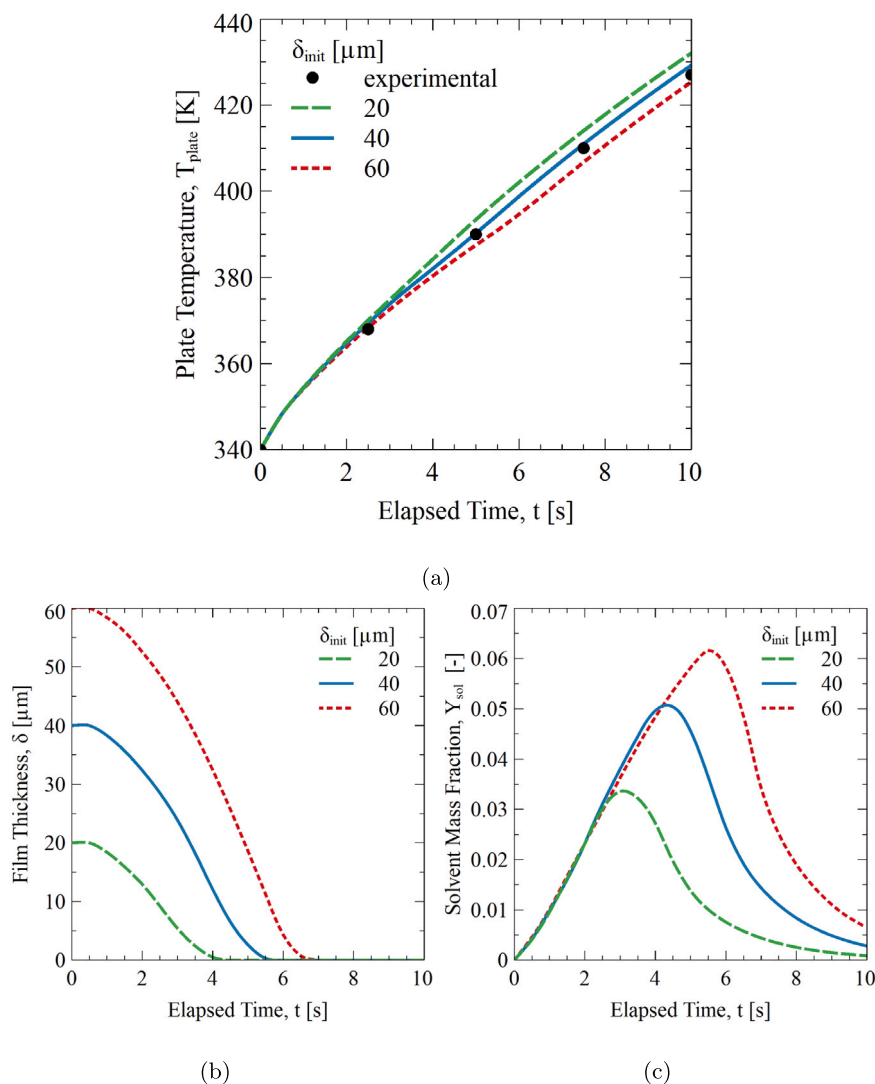

(a)

(b)

(c)

Fig. 16. Initial film thickness influence on the plate temperature (a), film thickness (b), and solvent mass fraction at the extraction section (c).
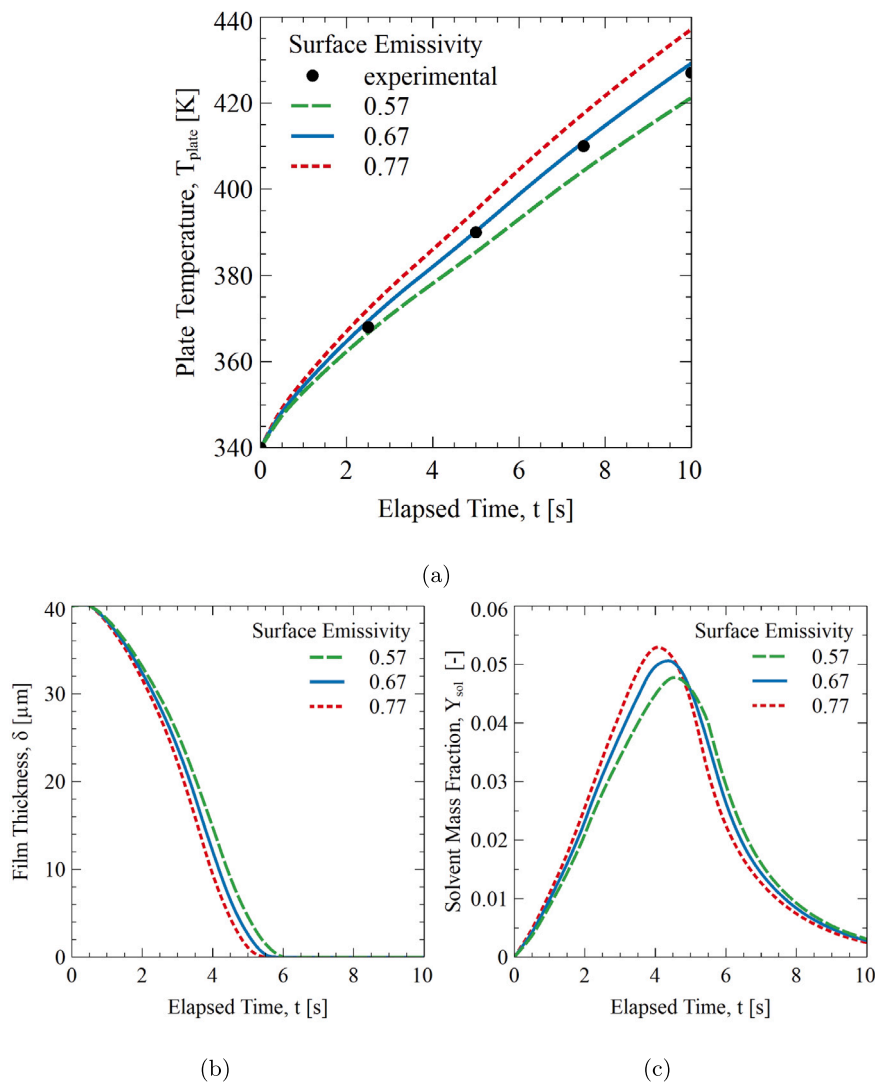
(a)

(b)

(c)

Fig. 17. Plate surface emissivity influence on the plate temperature (a), film thickness (b), and solvent mass fraction at the extraction section (c).

process of coil coating is continuous. Fig. 18 shows that for the initial film thickness of 20, 40, and 60 µm the model predicts the total film evaporation along 60%, 70%, and 75% of the total length of the oven, respectively.

Additionally, it is important to remark that a uniform incident radiation along the coil was obtained since a uniform source temperature was imposed. As seen previously, the incident radiation is higher along the first few meters of the coil – where the active radiant porous burners are located –, leading the previous approach (uniform incident radiation distribution) to become conservative since in practice, a total film evaporation is expected along a lower length of the oven. Therefore, to investigate the influence of a non-uniform incident radiation distribution on the film evaporation rate, a similar simulation was performed. Instead of imposing a constant source temperature, a non-linear source temperature was imposed to attain an equivalent distribution of the coil absorbed radiation of the nominal 3D simulation. The heating performance of the coil (without the film application) was firstly addressed and the calculated temperature profile was prescribed for prediction of film evaporation. Three different film thickness values were provided (initial film thickness) — 20, 40, and 60 µm. Figs. 19(a) and (b) present the temperature and film thickness profiles, respectively, along the longitudinal direction of the full-scale oven model. Fig. 19(b) shows that for the initial film thickness of 20, 40, and 60 µm, the model predicts the film total evaporation along 40%, 45%, and 50% of the
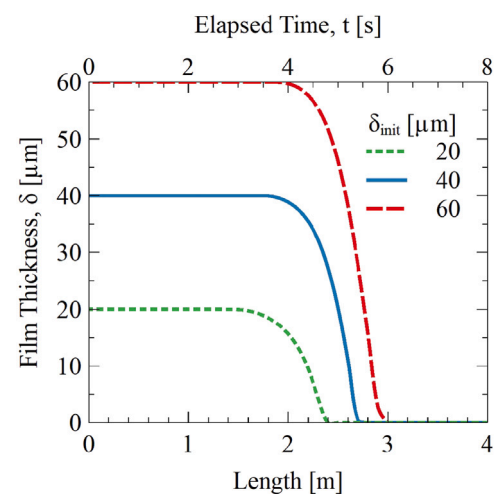

Fig. 18. Film thickness profiles along the full-scale oven longitudinal direction for different initial film thickness values.
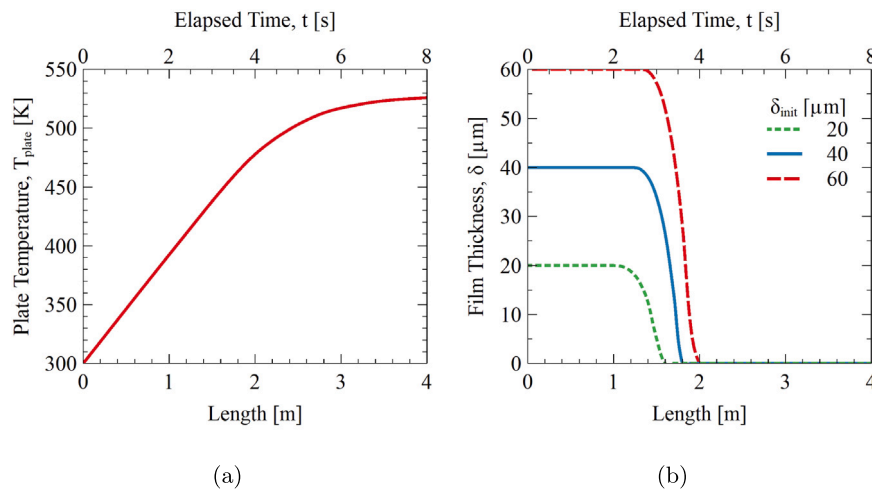
Fig. 19. Influence of the non-uniform incident radiation on the coil temperature profile (a) and film thickness profiles for different initial film thickness values (b).

total length of the chamber, respectively. Hence, the model is feasible to predict the complete evaporation of the film in the full-scale oven, even considering the most conservative approach. Hence, the nominal condition considered for the full-scale furnace operating is suitable to achieve a total evaporation (drying) of the applied coating.

5. Conclusions

In this work, the overall performance of a novel coil coating furnace operating with radiant porous burners was numerically investigated. In particular, the glass window thermal behavior during the oven operation was herein fully addressed, since the glass window thermal stability is a crucial aspect to ensure a long-term, safe, stable, and ultimately successful operation of the oven. The attachment of the cooling gas flow to the window was observed and the cooling system was able to reduce the average window temperature by about 164 K. Additionally, the hydrothermal performance of the RBS was characterized as well as the irradiation distribution at the coil top surface for different oven operating conditions. It was verified that the coil absorbed radiative power following the minimum value established. Moreover, the role played by the inertization chambers in isolating the COS atmosphere from the outside environment was investigated. It was verified that no solvent leaks into the environment and that the inertization chambers prevent the exterior oxygen from reaching the oven.

Furthermore, the heating performance of uncoated and coated metallic samples in the small-scale model of the oven was presented. The addition of the film lowers the heating rate of the plate. Moreover, the time to completely evaporate the film decreases with the increase of the temperature of the effective radiative heat source surface, the decrease of the initial film thickness, and with the increase of the surface emissivity. Finally, the complete evaporation of solvents from liquid film coatings within the full-scale oven was observed even considering the most conservative approach where the incident radiation is evenly distributed through the coil.

CRediT authorship contribution statement

Bruno A.C. Barata: Conceptualization, Data curation, Formal analysis, Investigation, Methodology, Software, Validation, Visualization, Roles/Writing – original draft, Writing – review & editing. **Beatriz S. Dias:** Conceptualization, Data curation, Formal analysis, Investigation, Methodology, Software, Validation, Visualization, Roles/Writing – original draft, Writing – review & editing. **Jorge E.P. Navalho:** Conceptualization, Data curation, Resources, Supervision, Roles/Writing – original draft, Writing – review & editing. **Michael Schneider:** Conceptualization, Data curation, Investigation. **Petra Weinbrecht:** Conceptualization, Data curation, Investigation. **Christof Weis:** Conceptualization, Data curation, Supervision. **Dimosthenis Trimis:** Conceptualization, Data curation, Funding acquisition, Project administration, Supervision. **José C.F. Pereira:** Conceptualization, Data curation, Funding acquisition, Project administration, Resources, Supervision.

Declaration of competing interest

The authors declare that they have no known competing financial interests or personal relationships that could have appeared to influence the work reported in this paper.

Data availability

Data will be made available on request.

Acknowledgments

References

[1] J. Sander, Coil Coating, 2019, http://dx.doi.org/10.1515/9783748602231.
[2] S. Rossi, F. Deflorian, J. Fiorenza, Environmental influences on the abrasion resistance of a coil coating system, Surf. Coat. Technol. 201 (2007) 7416–7424, http://dx.doi.org/10.1016/j.surfcoat.2007.02.008.
[3] G. Gupta, S. Pathak, A. Khanna, Anticorrosion performance of eco-friendly silane primer for coil coating applications, Prog. Org. Coat. 74 (2012) 106–114, http://dx.doi.org/10.1016/j.porgcoat.2011.11.023.
[4] S. Rossi, M. Calovi, D. Dalpiaz, M. Fedel, The influence of NIR pigments on coil coatings' thermal behaviors, Coatings 10 (2020) 514, http://dx.doi.org/10.3390/coatings10060514.
[5] A. Joudi, H. Svedung, M. Cehlin, M. Rönnelida, Reflective coatings for interior and exterior of buildings and improving thermal performance, Appl. Energy 103 (2013) 562–570, http://dx.doi.org/10.1016/j.apenergy.2012.10.019.
[6] S. Nameer, T. Deltin, P.-E. Sundell, M. Johansson, Bio-based multifunctional fatty acid methyl esters as reactive diluents in coil coatings, Prog. Org. Coat. 136 (2019) 105277, http://dx.doi.org/10.1016/j.porgcoat.2019.105277.
[7] B. Rosales, A. Di Sarli, O. Rincon, A. Rincón, C. Elsner, B. Marchisio, An evaluation of coil coating formulations in marine environments, Prog. Org. Coat. 50 (2004) 105–114, http://dx.doi.org/10.1016/j.porgcoat.2003.12.002.
[8] R. Knischka, U. Lehmann, U. Stadler, M. Mamak, J. Benkhoff, Novel approaches in NIR curing technology, Prog. Org. Coat. 64 (2) (2009) 171–174, http://dx.doi.org/10.1016/j.porgcoat.2008.09.015.

[9] I. Mabbett, J. Elvins, C. Gowenlock, P. Jones, D. Worsley, Effects of highly absorbing pigments on near infrared cured polyester/melamine coil coatings, Prog. Org. Coat. 76 (2013) 1184–1190, http://dx.doi.org/10.1016/j.porgcoat.2013.03.031.

[10] I. Mabbett, J. Elvins, C. Gowenlock, C. Glover, P. Jones, G. Williams, D. Worsley, Addition of carbon black NIR absorber to galvanised steel primer systems: Influence on NIR cure of polyester melamine topcoats and corrosion protection characteristics, Prog. Org. Coat. 77 (2) (2014) 494–501, http://dx.doi.org/10.1016/j.porgcoat.2013.11.015.

[11] T. Kolås, A. Røyset, M. Grandcolas, M. ten Cate, A. Lacau, Cool coatings with high near infrared transmittance for coil coated aluminium, Sol. Energy Mater. Sol. Cells 196 (2019) 94–104, http://dx.doi.org/10.1016/j.solmat.2019.03.021.

[12] S. Rossi, M. Calovi, D. Dalpiaz, M. Fedel, The influence of NIR pigments on coil coatings' thermal behaviors, Coatings 10 (6) (2020) http://dx.doi.org/10.3390/coatings10060514.

[13] K. Ohlsson, T. Bergman, P.-E. Sundell, T. Deltin, I. Tran, M. Svensson, M. Johansson, Novel coil coating systems using fatty acid based reactive diluents, Prog. Org. Coat. 73 (4) (2012) 291–293, http://dx.doi.org/10.1016/j.porgcoat.2010.11.018.

[14] R. Knischka, U. Lehmann, U. Stadler, M. Mamak, J. Benkhoff, Novel approaches in NIR curing technology, Prog. Org. Coat. 64 (2009) 171–174, http://dx.doi.org/10.1016/j.porgcoat.2008.09.015.

[15] J.W. Choi, W.P. Chun, S.H. Oh, K.J. Lee, S.I. Kim, Experimental studies on a combined near infrared (NIR) curing system with a convective oven, Prog. Org. Coat. 91 (2016) 39–49, http://dx.doi.org/10.1016/j.porgcoat.2015.11.004.

[16] D.A. Brennan, I. Mabbett, J. Elvins, N.P. Lavery, D.A. Worsley, Mathematical framework for predicting the thermal behaviour of spectrally selective coatings within an industrial near-infrared furnace, Eur. J. Comput. Mech. 25 (3) (2016) 294–308, http://dx.doi.org/10.1080/17797179.2016.1212628.

[17] R. Neno, B. Dias, J. Navalho, J. Pereira, Numerical simulation of heat removal from a window slab partition of a radiative coil coating oven, Energies 15 (2022) 2080, http://dx.doi.org/10.3390/en15062080.

[18] B.S. Dias, J.E.P. Navalho, J.C.F. Pereira, Multi-scale modeling and simulation of IR radiative drying for coil coating processes, Drying Technol. 40 (16) (2022) 3466–3482, http://dx.doi.org/10.1080/07373937.2022.2055055.

[19] Y. Yuan, S. Pan, T. Wang, L. Xia, Y. Liu, X. Wang, L. Li, T. Wang, Experimental and numerical investigations on curing a polyester-based powder coating by catalytic infrared radiation, Appl. Sci. 13 (4) (2023) http://dx.doi.org/10.3390/app13042187.

[20] T.H. Shih, W. Liou, A. Shabbir, Z. Yang, J. Zhu, A new k-ε eddy viscosity model for high Reynolds number turbulent flows, Comput. & Fluids 24 (1995) 227–238, http://dx.doi.org/10.1016/0045-7930(94)00032-T.

[21] NIST Chemistry WebBook, 2022, https://webbook.nist.gov/chemistry/. (Accessed: 31 October 2022).

[22] Ansys, Ansys Fluent Theory Guide, ANSYS, Inc, 2021, Release 2021 R2.

[23] C. Keramiotis, M. Katoufa, G. Vourliotakis, A. Hatziapostolou, M. Founti, Experimental investigation of a radiant porous burner performance with simulated natural gas, biogas and synthesis gas fuel blends, Fuel 158 (2015) 835–842, http://dx.doi.org/10.1016/j.fuel.2015.06.041.

[24] M. Fidalgo, M. Mendes, J. Pereira, An automated method for efficient multi-parametric analysis of porous radiant burner performance, Int. J. Therm. Sci. 163 (2021) 106851, http://dx.doi.org/10.1016/j.ijthermalsci.2021.106851.

[25] S.M. Vahidhosseini, J. Esfahani, K. Kim, Experimental study on the radiative heat transfer in a multi-hole porous radiant burner with internal combustion regime, Appl. Therm. Eng. 201 (2021) 117732, http://dx.doi.org/10.1016/j.applthermaleng.2021.117732.